energies

MDPI

Article

A Dual-Factor Defrosting Model for Air-Source Heat Pumps Considering Ambient Temperature and Compressor Frequency

Xuyan Xu [1], Tao Zhang [2,*], Dongming Li [2], Wanchun Sun [2], Zhijiang Wu [2] and Yansheng Xu [2,*]

[1] Department of Industrial Engineering, Tsinghua University, Beijing 100084, China; xuxy19@mails.tsinghua.edu.cn
[2] School of Energy and Automotive Engineering, Shunde Polytechnic University, Foshan 528000, China
* Correspondence: zhangtao5524@163.com (T.Z.); 10222@sdpt.edu.cn (Y.X.)

Abstract

This study presents a novel investigation into the coupled effects of ambient temperature and compressor frequency on frosting behavior and thermal performance of inverter-driven air-source heat pumps (ASHPs) under low-temperature, high-humidity conditions. Unlike previous studies that focused on single environmental parameters, this work systematically explores temperature–frequency coupling. Experiments were conducted on a 3-HP DC inverter low-ambient-temperature ASHP unit using a multi-climate simulated enthalpy difference test bench. Single-factor analysis shows that frosting is most severe at 0 °C, where the frost growth rate peaks. Regarding compressor frequency, the coefficient of performance (COP) initially increases and then decreases with frequency. The maximum COP occurs near 45 Hz, representing the optimal energy efficiency balance in this experimental system. Sensitivity analysis demonstrates that relative humidity contributes less than 5% to performance degradation at the critical 10% COP reduction point. Thus, ambient temperature and compressor frequency are the core determinants of defrosting timing. A dual-factor prediction model for the critical defrosting air-to-coil temperature difference (ΔT) is developed using temperature (t) and frequency (f) as independent variables. Validation confirms that the model maintains prediction error within 10% under both single-factor and multi-factor coupling conditions. Collectively, this research quantifies the coupled effects of ambient temperature and compressor frequency on frosting performance and provides a novel theoretical framework for precise defrosting control in inverter ASHPs based on performance attenuation.

Keywords: air-source heat pump; frosting characteristics; compressor frequency; coupled effects; dual-factor model; precise defrosting

Check for updates

Academic Editor: Mahmoud Bourouis

Received: 17 April 2026
Revised: 27 May 2026
Accepted: 29 May 2026
Published: 10 June 2026

Copyright: © 2026 by the authors. Licensee MDPI, Basel, Switzerland. This article is an open access article distributed under the terms and conditions of the Creative Commons Attribution (CC BY) license.

1. Introduction

As a high-efficiency and environmentally friendly heating technology, air source heat pumps (ASHP) have been widely used in building heating, industrial and agricultural drying, and other fields due to their advantages such as convenient installation, high energy efficiency ratio and strong applicability. Against the backdrop of the "dual carbon" target, promoting the large-scale application of air source heat pumps in cold and frigid regions has become one of the important paths for energy conservation and emission reduction in the building sector [1]. According to statistics, the sales of air source heat pumps in China reached RMB 22.7 billion in 2021, an increase of nearly 25% year-on-year [2], showing a continuous growth trend. However, during practical operation, frost can readily

accumulate on the evaporator surface under conditions of low ambient temperature and high relative humidity. This frost accumulation leads to increased heat transfer resistance and reduced airflow, consequently degrading the unit's heating capacity and escalating energy consumption. In severe cases, it can precipitate frequent defrosting cycles and even interrupt heating provision, thereby compromising operational reliability [3]. This technical bottleneck restricts the efficient and stable operation of air source heat pumps in low-temperature and high-humidity environments and has become a research hotspot of common concern in academia and industry.

Accurate judgment of the defrost node is the core issue affecting the operating efficiency and economy of air source heat pumps. Ma et al. [2] clearly pointed out in their latest review that the key challenge of defrost control is how to accurately identify the degree of frost and optimize the defrost start-stop logic. Suboptimal defrosting decisions, whether premature or delayed, significantly increased system energy consumption and compromised component reliability. The study by Klingebiel et al. [4] further quantified this impact, demonstrating that a deviation of 20 min from the optimal defrost start time could lead to a system efficiency reduction of up to 9.1%. If defrost is too early, the unit will fall into an ineffective operating state of "defrosting without frost", resulting in energy waste and unnecessary heating interruption. Conversely, if defrosting was initiated too late, excessive frost accumulation severely deteriorated the evaporator's heat exchange performance, leading to a significant attenuation of heating capacity and potentially causing safety issues such as compressor liquid hammer. Therefore, accurately identifying the critical defrosting point and achieving on-demand defrosting had become a cutting-edge topic in ASHP technology research.

Domestic and international scholars have conducted in-depth research on defrosting control strategies. Traditional defrosting control methods mainly relied on timers and temperature-time difference logic. Their simple structure and low cost led to widespread application in early products. However, because these methods could not adapt to complex and variable climatic conditions, their control accuracy was limited, resulting in significant efficiency losses. The study by Klingebiel et al. [4] showed that compared to an optimal defrost strategy, the efficiency loss of a timer-based control strategy (60 min interval) could reach 16.0%. While demand-based control reduced the loss to 7.0%, parameter trade-offs still existed under different frosting intensity conditions, limiting the overall system efficiency improvement.

To overcome the limitations of traditional methods, researchers have devoted efforts to developing refined control strategies based on thermodynamic parameters. Liu et al. proposed a novel frosting suppression control strategy for variable-speed air source heat pumps based on condensing-frosting performance maps, which optimises operating parameters to effectively suppress frosting while maintaining a high COP [5]. Compared with conventional control, this strategy increases the cyclic heating duration by 157.68% and reduces the daily defrosting frequency, defrosting duration, and defrosting energy consumption by 59.09%, 36.30%, and 32.96%, respectively [5]. Li et al. [6] developed a prediction model for the optimal defrosting initiation time for air source heat pumps with different configurations and operating modes. By establishing a cubic function relationship between a comprehensive index of configuration and operation (CICO) and the optimal initiation time, the model can predict the defrosting start time for different units. When the CICO value increases from 3.14 to 22.44, the optimal defrosting initiation time increases from 22 min to 148 min. Tang et al. experimentally studied the influence of frosting on heat pump performance through the operating characteristics of the outdoor fan and proposed a novel time-current-temperature difference (T-I-T) defrosting control method. The results show that the defrosting current threshold decreases with decreasing frosting severity; after

applying this method, the defrosting frequency is reduced by 39.80%, and the average COP is increased by 10.60% [7]. Chung et al. [8] used a differential pressure sensor to monitor the pressure difference inside and outside the evaporator and found that the average pressure difference at the bottom of the evaporator could most accurately reflect the frost growth. By dimensionlessly processing the critical pressure difference, this method can be effectively applied to different fan speeds and heat exchanger specifications. In nine sets of verification experiments under different outdoor conditions, its root mean square error of prediction was as low as 5.5%.

In recent years, the rapid development of artificial intelligence technology has provided new ideas for breaking through the dependence on traditional models. Klingebiel et al. [9] proposed a self-optimizing defrosting start controller based on deep reinforcement learning, which can generate control rules autonomously by interacting with the environment using only the measurement values of standard temperature sensors. Hardware-in-the-loop tests were conducted under dynamic environmental conditions. The results show that the seasonal energy coefficient of the proposed controller is 7.1% higher than that of the time-type controller and 9.1% higher than that of the demand-type controller. Additionally, the heating capacity is increased by 4.9%. Under the fault condition of simulated airflow blockage, the efficiency is improved by 16.6% through an online learning adaptive adjustment strategy. Guo et al. [10] proposed a data-driven evaluation method for defrosting effect based on the heating capacity decay model. The frost state is identified by monitoring the heating capacity decay, and an on-demand defrosting control strategy is developed based on a fully connected neural network. The degree of frost is divided into six categories to achieve real-time identification. After application, the defrosting frequency is reduced by 66.3%, and the power consumption is reduced by 6.0%.

The development of image processing technology provides a more intuitive means of quantifying the degree of frost. Wang et al. [11] proposed a defrosting start control method based on image grayscale recognition. They developed corresponding image recognition equipment and control strategies. Experimental results showed that the defrosting accuracy of the method reached 93.33% in complex and variable environments. Compared with traditional temperature-time control, the defrosting accuracy was improved by 42.86%, and the average COP of the unit was improved by 36.60%. Zheng et al. [12] applied multi-threshold segmentation technology to divide the grayscale image into frost-free area, moderate frost area and heavy frost area, introduced the frost coefficient P (0~1) to evaluate the degree of frost, set P = 0.3 to start defrosting and P = 0.05 to end defrosting. Experiments verified that the method is applicable to a variety of outdoor environments.

While the aforementioned studies have advanced defrosting control technology from different perspectives, a key gap remains in current research. Most existing studies treat ambient temperature and relative humidity as the primary inputs. The unit's own operating parameters—especially compressor frequency—are largely ignored or considered as constants. Compressor frequency directly affects refrigerant mass flow rate, evaporation temperature, and heat exchange performance. Therefore, it profoundly influences frost growth rate and the timing of performance deterioration. A few recent studies have begun to acknowledge the role of frequency. For example, Wei et al. [13] studied the frosting performance of variable-frequency ASHPs under different climatic regions. They found that frequency significantly alters the frosting map boundaries. However, they did not develop a quantitative model linking frequency to the critical defrosting point. Consequently, a systematic exploration of the coupling relationship between compressor frequency, frost dynamics, and the defrosting critical point is still lacking. This current research status restricts the accuracy of defrosting control. It also limits the full release of the performance potential of inverter-driven ASHPs.

In view of this, an enthalpy difference laboratory capable of accurately simulating various climatic conditions was built in this study. Using a 3 HP DC inverter low-ambient-temperature air-source heat pump (chilled water) unit as the research object, frosting experiments were systematically conducted under different ambient temperatures, compressor frequencies, and relative humidity conditions. By analyzing the frost layer growth pattern and the variation characteristics of performance parameters such as heating capacity, power consumption, and COP of the unit, the frosting characteristics under the coupling effect of temperature and frequency and their impact mechanism on system performance were revealed. The main contributions of this work are threefold. First, the coupled effect of ambient temperature and compressor frequency on the critical defrosting air-to-coil temperature difference (ΔT) is quantified for the first time. Single-factor analysis shows that frosting is most severe at 0 °C and that the COP peaks at around 45 Hz, beyond which energy efficiency declines. Second, a novel dual-factor prediction model $\Delta T = f(t, f)$ that explicitly includes a cross-term to capture the temperature–frequency interaction is proposed. The model achieves high accuracy ($R^2 = 0.908$, RMSE = 0.82 °C) with a prediction error below 10%. Third, the model is validated under both single-factor and multi-factor coupled conditions (varying humidity and frequency), and it is demonstrated that relative humidity has a negligible effect (<5%) on the critical ΔT, confirming that temperature and frequency are the core determinants of defrosting timing. This research fills the gap in existing defrosting control strategies that neglect the influence of compressor frequency, providing a theoretical framework and a practical engineering tool for achieving truly intelligent, precise, and performance-attenuation-based defrosting control in inverter air-source heat pumps.

2. Experimentation

2.1. Experimental Platform

To conduct in-depth research on the operating characteristics and performance of air-source heat pump units under different environments, this study constructed a comprehensive experimental platform based on the enthalpy difference (water system) laboratory. This experimental platform aims to simulate diverse climatic conditions and load scenarios, enabling high-precision measurement and analysis of key performance parameters of the unit. The overall platform integrates functions such as environmental simulation, load simulation, data acquisition, and unit monitoring and control, providing a reliable foundation for subsequent systematic experiments. The overall appearance of the experimental platform is shown in Figure 1.



Figure 1. External view of the experimental prototype.

2.2. Air Source Heat Pump Unit

The experiment used a 3HP DC inverter low-ambient-temperature air-source heat pump (chilled water) (TMEGA, Foshan, China) unit as the test object. This unit features full DC inverter control, allowing independent adjustment of compressor and fan speeds as well as the electronic expansion valve opening. This facilitates the flexible setting of different operating parameters during the experiment to investigate their impact on unit performance. The system uses R410A as the refrigerant. The main performance parameters of the unit are shown in Table 1. It has a compact structure, high control precision, and is suitable for stable operation over a wide temperature range.

Table 1. Parameter of air source heat pump unit.

Parameter	Numerical Values
Unit power supply specifications	220 V/50 Hz
Rated heating capacity (outdoor −12°C, outlet water 55°C)	6.1 kW
Rated heating input power (outdoor −12°C, outlet water 55°C)	2.52 kW
Rated heating current (outdoor −12°C, outlet water 55°C)	11.45 A
Rated outlet water temperature	41 °C
Maximum water temperature	60 °C
Scope of work	−35~45 °C
Protection level	IP × 4
Unit noise	≤62 dB
Differential pressure between inlet and outlet water of the unit	30 kPa
Rated circulating water volume	1.09 m^3/h
External dimensions	900 × 365 × 865 mm
Main unit control size	DN25
Equipment weight	110 kg

2.3. Environmental Simulation System

To accurately simulate the operating environment of an air-source heat pump, the experimental setup includes two independent environmental simulation chambers: an indoor chamber and an outdoor chamber. The indoor temperature can be adjusted within the range of 5–50 °C, while the outdoor temperature range is −25–55 °C, and the relative humidity can be controlled between 20% and 95%. The system employs a PLC and intelligent power regulator for coordinated control, combined with electric heating and humidification devices, to ensure rapid and stable operation, providing realistic and controllable atmospheric conditions for unit performance testing.

2.4. Water System Simulation

To simulate actual water-side load, an independent water circulation testing system was installed on the outdoor side of the test bench. This system allows for continuous flow rate adjustment within the range of 0–7 m^3/h and uses turbine flow meters and resistance thermometers to monitor the supply and return water temperatures and flow rates in real time, thereby accurately calculating the unit's heating capacity and energy efficiency. The introduction of the water system enables the test bench to be suitable not only for air-side performance studies but also for comprehensively evaluating the unit's thermal performance on the water side.

2.5. Data Acquisition and Measurement System

To ensure the comprehensiveness and accuracy of experimental data, the experimental platform is equipped with a multi-parameter synchronous acquisition system. This system includes temperature and humidity sensors, pressure transmitters, thermocouples, an energy analyzer, and a high-precision flow meter, covering various key parameters from

the air, water, and electrical sides (Table 2). All sensors are rationally arranged according to measurement specifications and are monitored and recorded in real time via a data acquisition instrument and host computer software, providing a reliable basis for subsequent data analysis.

Table 2. Parameters of main data acquisition equipment.

Equipment	Model/Type	Measurement Parameters	Accuracy/Range	Sampling Interval
Platinum resistance thermometer	Pt-100	air temperature and humidity	±0.1 °C	real time
Differential pressure transmitter	—	wind static pressure	0–300 Pa	real time
Turbine flow meter	—	Water flow	0–3 m^3/h, ±0.5% FS	6 s
thermocouple	K type	Coil temperature	−200~260 °C	6 s
Electrical parameter instrument	—	Voltage, current, power	±0.5%	real time
Data acquisition system	Industrial PC + Data Acquisition Card	Multi-channel synchronous acquisition	16-bit resolution	

2.6. Experimental Conditions

The variables in this experiment included ambient temperature, humidity, and compressor frequency. The experimental conditions were set using a single variable method. The temperature was set to 6 °C, 3 °C, 0 °C, −3 °C, −6 °C, −9 °C, and −12 °C, for a total of 7 conditions. The compressor frequency was set to 30 Hz, 45 Hz, 60 Hz, 76 Hz, and 90 Hz, for a total of 5 conditions. The humidity was set to 70%, 75%, 80%, and 85%. The specific experimental conditions for the temperature, compressor frequency, and humidity groups are shown in Tables 3, 4, and 5, respectively. In addition, in order to fully observe the changes in the unit's COP, the unit's original variable frequency control and defrosting settings were turned off, and it was operated in fixed frequency mode with manual defrosting.

Table 3. Temperature condition.

Experiment Number	Temperature (°C)	Other Variable Value
1-1	6	Frequency: All frequency operating conditions Relative humidity: 85%
1-2	3	
1-3	0	
1-4	−3	
1-5	−6	
1-6	−9	
1-7	−12	

Table 4. Frequency operating condition.

Experiment Number	Frequency Setting (Hz)	Other Variable Value
2-1	30	Temperature: All temperature conditions Relative humidity: 85%
2-2	45	
2-3	60	
2-4	76	
2-5	90	

Table 5. Relative humidity operating condition.

Experiment Number	Relative Humidity (%)	Other Variable Value
3-1	70	Temperature: 3 °C, 0 °C, −6 °C Frequency: 76 Hz
3-2	75	
3-3	80	
3-4	85	

2.7. Data Processing

When studying unit performance, frosting characteristics and performance indicators cannot usually be directly derived from measured data. Therefore, it is necessary to perform formula conversion and processing on the measured data in order to accurately assess the unit's heating capacity and energy efficiency. Heating capacity and coefficient of performance (COP), as key parameters for measuring unit performance, rely on a comprehensive analysis of variables such as environmental conditions and unit operating status for calculation.

The unit's heating capacity is determined by the water flow rate and supply and return water temperatures of the water system, and its calculation formula is shown in Equation (1):

$$Q = c_w \rho_w V_w (t_{wg} - t_{wh}) \quad (1)$$

where Q— heat output of the unit (kW);

c_w—specific heat capacity of water ((kJ/(kg·°C));
ρ_w—water density (kg/m^3);
V_w—water system volumetric flow rate (m^3/s);
t_{wg}—water supply temperature (°C);
t_{wh}—return water temperature (°C).

The COP (coefficient of performance) of a heat pump is an indicator of its energy efficiency. It represents the ratio of the heat provided by the heat pump per unit time to the power consumed. Its calculation formula is shown in Equation (2):

$$COP = Q/W \quad (2)$$

where Q—heat output of the unit (kW);

W—power consumed by the unit (kW).

During the frosting process of a heat pump, the air-to-coil temperature difference (ΔT) is a key physical quantity that directly reflects the actual heat exchange state. However, the coil surface temperature measurement is easily affected by the location of the measuring point, resulting in variations. In contrast, the pressure fluctuation range at the evaporator outlet is smaller, providing a more stable and accurate reflection of the refrigerant saturation temperature within the coil. Therefore, this paper selects the evaporator outlet pressure as the observation basis and uses the pressure-temperature correspondence to calculate a more representative coil temperature, thereby calculating the air-to-coil temperature difference ΔT. The calculation formula is shown in Equation (3):

$$\Delta T = t\ (^\circ\mathrm{C}) - \left(\frac{-2107.935}{ln((P+1) \times 100,000) - 21.8205} - 256.2377\right) \quad (3)$$

where t —ambient temperature (°C).

P—gauge pressure (bar) at the evaporator outlet.

2.8. Uncertainty Analysis

To evaluate the reliability of the experimental results, an uncertainty analysis was performed for the key derived parameters: heating capacity (Q), coefficient of performance (COP), and air-to-coil temperature difference (ΔT). The measurement uncertainties of the primary instruments (Table 2) were propagated using the root-sum-square (RSS) method, assuming all input quantities are independent. The combined standard uncertainty $u_c(y)$ for a derived quantity $y = f(x1, x2, \ldots, xn)$ is calculated as

$$u_c(y) = \sqrt{\sum_{i=1}^{n} \left(\frac{\partial f}{\partial x_i} \cdot u(x_i) \right)^2} \tag{4}$$

where $u(x_i)$ is the standard uncertainty of the input x_i, and $\frac{\partial f}{\partial x_i}$ is the sensitivity coefficient.

The expanded uncertainty U is then obtained by multiplying $u_c(y)$ by a coverage factor k = 2, corresponding to a confidence level of approximately 95%:

$$U = k \cdot u_c(y) \tag{5}$$

Heating capacity Q is given by $\mathrm{Q} = \mathrm{c_w \rho_w V_w (t_{wg} - t_{wh})}$. The relative combined uncertainty is

$$\frac{u_c(Q)}{Q} = \sqrt{\left(\frac{u(V_w)}{V_w} \right)^2 + \left(\frac{u(\Delta t_w)}{\Delta t_w} \right)^2} \tag{6}$$

where $\Delta t_w = t_{wg} - t_{wh}$. The turbine flow meter has an accuracy of ±0.5% of full scale (0–3 $\mathrm{m^3/h}$), yielding a standard uncertainty

$$u(V_w) = \frac{0.005 \times 3}{\sqrt{3}} \approx 0.00866\,\mathrm{m^3/h}$$

for a rectangular distribution. The Pt-100 sensors have an accuracy of ±0.1 °C each, so

$$u(\Delta t_w) = \frac{\sqrt{0.1^2 + 0.1^2}}{\sqrt{3}} \approx 0.0816\ ^\circ\mathrm{C}$$

The resulting relative expanded uncertainty for Q is approximately ±5.1% (k = 2).

Coefficient of performance $COP = Q/W$. The relative combined uncertainty is

$$\frac{u_c(\mathrm{COP})}{\mathrm{COP}} = \sqrt{\left(\frac{u_c(Q)}{Q} \right)^2 + \left(\frac{u(W)}{W} \right)^2} \tag{7}$$

The electrical parameter instrument has an accuracy of ±0.5% of the reading (assumed rectangular distribution). The relative standard uncertainty of W is $0.005/\sqrt{3} \approx 0.00289$. Combining with the uncertainty of Q gives a relative expanded uncertainty for COP of approximately ±6.2% (k = 2).

Air-to-coil temperature difference $\Delta T = t - T_{\mathrm{coil}}(P)$, where t is ambient temperature and $T_{\mathrm{coil}}(P)$ is the saturation temperature corresponding to the evaporator outlet pressure P. The combined uncertainty is

$$u_c(\Delta T) = \sqrt{u(t)^2 + u(T_{coil})^2} \tag{8}$$

The ambient temperature uncertainty $u(t) = 0.1/\sqrt{3} \approx 0.0577$ °C. The pressure transducer accuracy is ±0.5% FS (0–300 Pa), giving a standard uncertainty $u(P) = (0.005 \times 300)/\sqrt{3} \approx 0.866$ Pa. Using the saturation pressure-temperature relation for R410A, this translates to an uncertainty in T_{coil} of about ±0.3 °C (after calibration). Thus

$u_c(\Delta T) \approx \sqrt{0.0577^2 + 0.173^2} \approx 0.182$ °C (assuming a typical value of $0.3/\sqrt{3} \approx 0.173$ °C for $u(T_{coil})$. The expanded uncertainty for ΔT is approximately ±0.36 °C ($k = 2$).

All performance changes reported in this paper are significantly larger than the corresponding measurement uncertainties, confirming the statistical significance of the observed trends. This uncertainty analysis demonstrates that the experimental data are reliable for validating the proposed dual-factor defrosting model.

3. Results and Discussion

3.1. The Influence of Air Temperature

Figure 2 shows the growth characteristics of frost layer thickness over time under various temperature conditions. Seven ambient temperature conditions were set: 6 °C, 3 °C, 0 °C, −3 °C, −6 °C, −9 °C, and −12 °C. The compressor frequency was 76 Hz, and the relative humidity was 85%. As can be seen from the figure, under different temperature conditions, the frost layer thickness exhibits a rapid initial growth followed by a slower growth over time, until the frost layer completely fills the gaps between the fins. This growth characteristic is determined by the physical mechanism of the frosting process: in the initial stage of frosting, the frost layer grows rapidly mainly in the vertical direction. This is because the fin surface temperature is low, and water vapor in the air quickly condenses into frost, leading to a rapid increase in frost layer thickness. As the frost layer thickens, the gaps between the fins are gradually filled, increasing thermal resistance, restricting airflow, and reducing the efficiency of water vapor transport. Therefore, the growth rate of the frost layer gradually slows down until the frost layer completely seals the gaps between the fins, at which point the frost layer growth tends to saturate. At lower ambient temperatures (−12 °C, −9 °C), the frost layer grows faster, especially at temperatures close to freezing (0 °C), where the water vapor content in the air is higher, the condensation rate is faster, and the frost layer can more easily cover the fin gaps in a shorter time. At higher temperatures (6 °C), the frost layer grows more slowly, and frost only begins to form on the surface after 40 min of operation. This is because the coil surface temperature is higher at this temperature, requiring a longer time to reach the conditions for frosting.

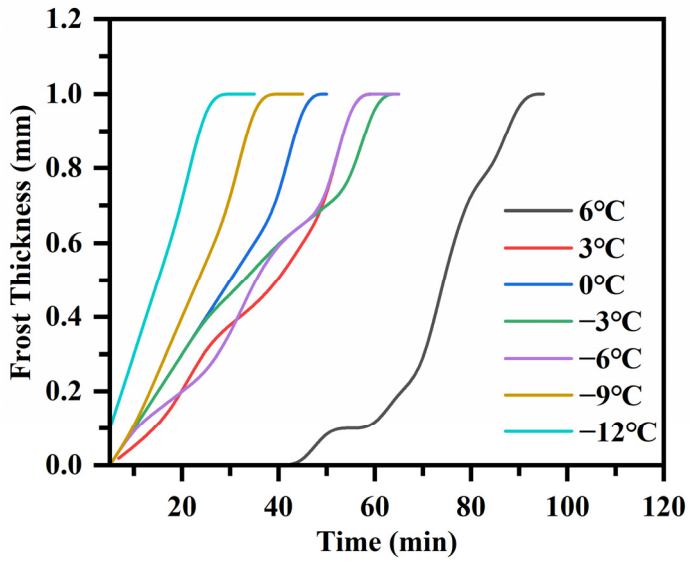


Figure 2. Changes in frost thickness with operating time under different ambient temperatures. The compressor frequency was 76 Hz, and the relative humidity was 85%.

Figure 3 shows the changes in unit heating capacity, power consumption, COP, and air-coil surface temperature difference over operating time under various temperature conditions. Seven temperature conditions were set: 6 °C, 3 °C, 0 °C, −3 °C, −6 °C, −9 °C, and −12 °C. The compressor frequency was 76 Hz, and the relative humidity was 85%. Figure 3a illustrates the change in unit heating capacity under different ambient temperatures. The initial heating capacity is mainly determined by the ambient temperature, showing a clear negative correlation. The lower the temperature (e.g., −12 °C), the worse the initial heating capacity, and the more gradual the decrease in heating capacity. At 6 °C, the frosting process is slow, and the heating capacity remains stable in the early stages due to the absence of frosting, only showing a significant decrease after a considerable period of operation. As operating time progresses, for a short period after frosting begins, the heating capacity briefly increases slightly due to the increased heat exchange capacity of the fins caused by the frost layer. Afterward, as the frost layer thickens, the heating capacity begins to decline rapidly. As can be seen from the figure, frosting is most severe at 0 °C, and the heating capacity declines the fastest. Ultimately, the heating capacity of all frosting conditions continued to decrease over time until the frost layer stabilized, at which point the rate of decrease gradually slowed down.

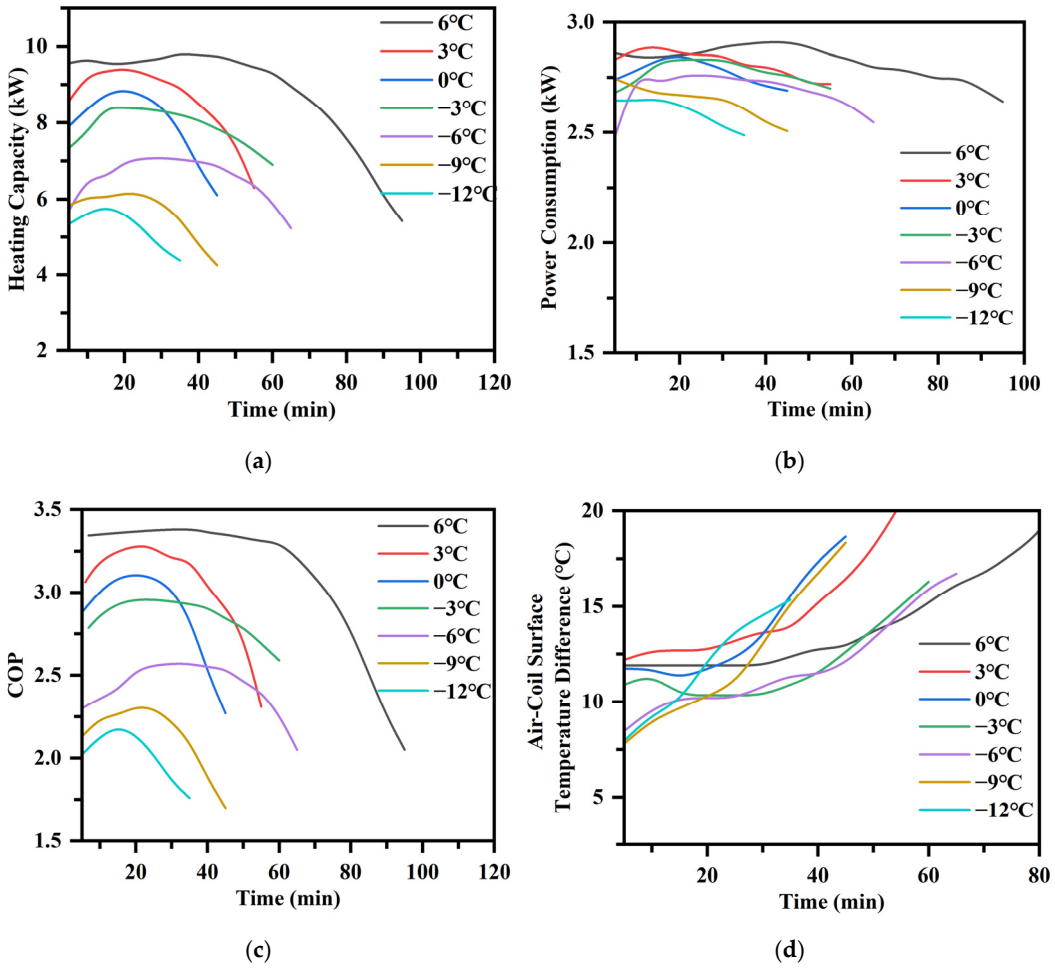


Figure 3. Changes in (**a**) unit heating capacity, (**b**) unit power consumption, (**c**) COP, and (**d**) temperature difference between air and coil surface over operating time at different ambient temperatures (6 °C, 3 °C, 0 °C, −3 °C, −6 °C, −9 °C, and −12 °C). The compressor frequency was 76 Hz, and the relative humidity was 85%.

Figure 3b depicts the power consumption characteristics of the heat pump during the frosting process at different ambient temperatures. Overall, the unit's power consumption

shows a slow decreasing trend as the frosting process progresses. The underlying mechanism is that the accumulation of frost increases the thermal resistance, leading to a decrease in evaporation temperature and thus reducing the refrigerant mass flow rate; consequently, the compressor's power consumption decreases.

Figure 3c plots COP against time (min) for each ambient temperature. In general, COP first increases slightly and then decreases gradually over time due to frost accumulation. Since the power consumption fluctuates gently throughout the entire frosting cycle, its changes have a weak impact on the system's COP (Figure 3b), making the COP trend mainly dependent on the decay of heating capacity. For temperatures above 0 °C (6 °C and 3 °C), the maximum occurs at the earliest time (10 min), because mild frosting quickly increases thermal resistance without any beneficial surface roughening effect. At temperatures below 0 °C, the maximum often appears at 20 min, indicating a short initial period of performance improvement before frosting dominates. This delay is caused by the fact that early-stage frost formation at subzero temperatures can enhance heat transfer by increasing surface roughness and turbulence, temporarily offsetting the insulation effect. The most severe relative COP drop (55.0%) occurs at −9 °C, followed by −12 °C (50.0%). The particularly large drop at −9 °C is attributed to a combination of a very low evaporating temperature and sustained frost growth, which leads to dense, highly insulating frost that accumulates rapidly after the initial enhancement period. At 0 °C, the drop is 34.6%, which is less than at −3 °C and below. This is because near 0 °C, frost grows quickly but remains relatively porous, causing less severe performance degradation than the dense frost formed at lower temperatures.

Figure 3d illustrates the variation in the temperature difference between the air and the coil surface during the defrosting process of the heat pump under different ambient temperatures. It can be seen that as time increases, the temperature difference between the coil and the air gradually increases, and the rate of increase accelerates. This is because as the frost layer continues to accumulate, the increased resistance in the air duct leads to a significant decrease in airflow, resulting in a reduction in the unit's heating capacity and a decrease in the evaporation temperature. The rising temperature difference between the coil and the air, and its accelerating rate, reflects the sharp deterioration of thermal performance in the later stages of defrosting. Furthermore, the rate of increase in temperature difference varies significantly under different ambient temperatures. For example, the rate of increase is higher at 0 °C than under other conditions, which is consistent with the pattern of frost layer thickness growth mentioned earlier at that temperature.

Figure 4 illustrates the relationship between the coefficient of performance (COP) of an air-source heat pump unit and the air-to-coil temperature difference (ΔT) at a fixed compressor frequency. The figure contains five subplots corresponding to different compressor frequency conditions: (a) 30 Hz, (b) 45 Hz, (c) 60 Hz, (d) 76 Hz, and (e) 90 Hz. Taking the 76 Hz condition in Figure 4c as an example, the COP initially increases and then decreases with increasing air-to-coil temperature difference. When the temperature difference is small, the COP gradually increases and reaches a peak at a certain critical point. This upward phase can be attributed to the increased surface roughness of the fins due to the frost layer distribution during the initial frosting stage, which enhances airflow turbulence and heat exchange area, thereby improving heat exchange performance. However, when the temperature difference exceeds this critical value, the COP begins to decrease. This phenomenon can be attributed to the significant deterioration of evaporator heat exchange conditions caused by excessively large temperature differences, leading to a decrease in heating efficiency. Meanwhile, a decrease in ambient temperature also leads to a decrease in COP, especially at −12 °C, where the COP drop is more significant. This is mainly because the evaporator is more prone to frosting in low-temperature environments, resulting in

a further decrease in heat transfer efficiency. Furthermore, as shown in Figure 4a,b, when the ambient temperature is 6 °C, the COP does not show a clear variation with temperature difference, fluctuating within an air-to-coil temperature difference range of 8–10 °C. This is because when the compressor operates at low frequencies of 30 Hz and 45 Hz, the evaporator basically does not frost at 6 °C; thus, the unit performance tends to be stable with small fluctuations. However, at the same ambient temperature of 6 °C but with other frequencies (e.g., 60 Hz, 76 Hz, 90 Hz), frosting occurs, leading to a decrease in COP after an initial period. To cover a wide temperature range and achieve broader applicability, the rated condition of 76 Hz was selected for subsequent fixed-frequency studies to investigate the effects of other factors. This frequency provides more representative data for evaluating the coupled effects of ambient temperature and compressor frequency across different operating conditions.

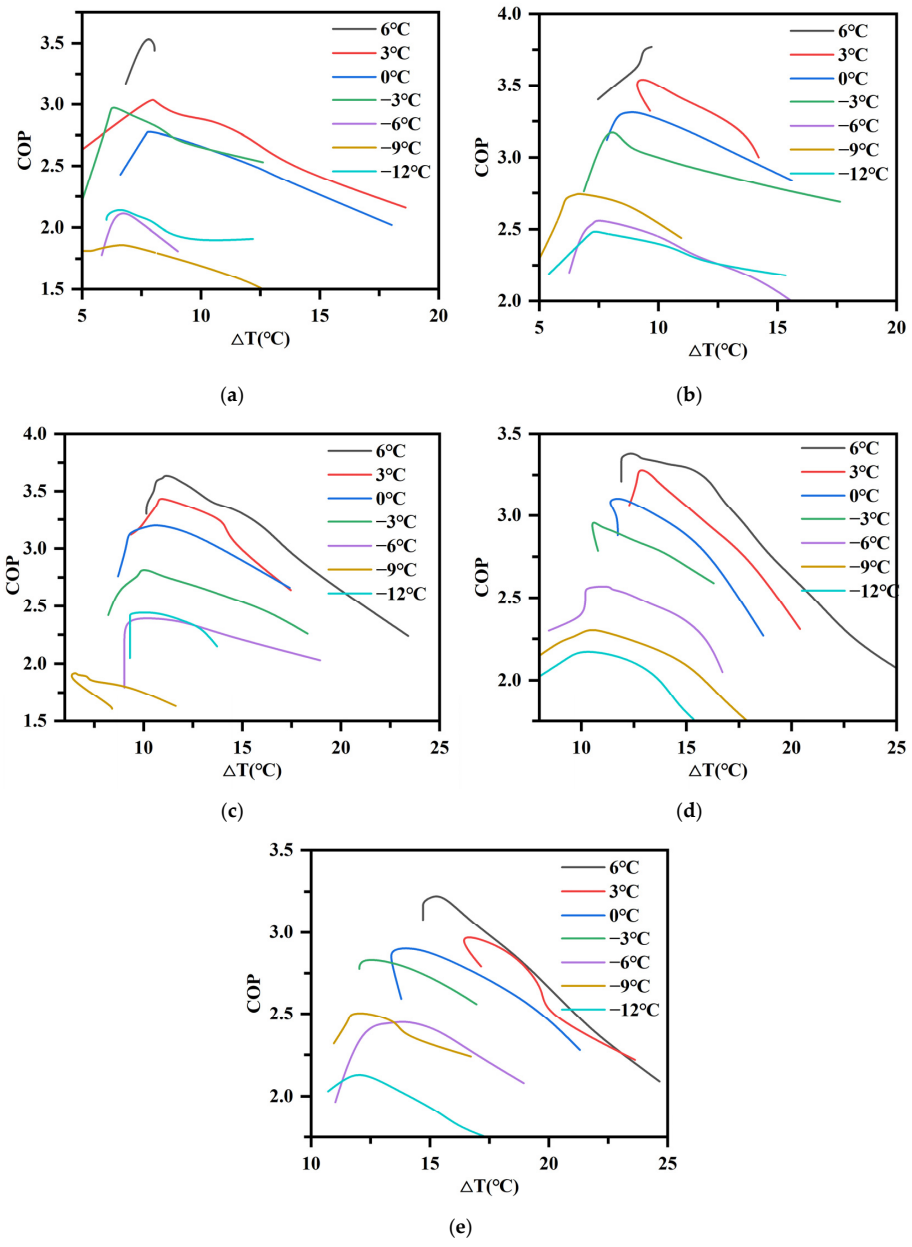


Figure 4. Changes in COP of the unit with air-to-coil temperature difference (ΔT, temperature difference between the ambient temperature (T_a) and the coil surface temperature (T_F) converted from the evaporator outlet pressure) at different ambient temperatures (6 °C, 3 °C, 0 °C, −3 °C, −6 °C, −9 °C, and −12 °C) at a fixed frequency: (**a**) 30 Hz, (**b**) 45 Hz, (**c**) 60 Hz, (**d**) 76 Hz, (**e**) 90 Hz.

3.2. The Influence of Compressor Frequency

Figure 5a shows the characteristics of frost thickness variation over time under different compressor frequencies. Five frequency groups were set: 30 Hz, 45 Hz, 60 Hz, 76 Hz, and 90 Hz, with an ambient temperature of 0 °C and a relative humidity of 85%. As can be seen from Figure 5a, under different frequency conditions, the frost thickness generally shows a trend of rapid initial growth followed by a gradual slowdown until the frost completely fills the fin gaps. This phenomenon is closely related to the physical mechanism of the frosting process: in the initial stage of frosting, higher compressor frequencies typically correspond to larger refrigerant flow rates and lower evaporation temperatures, resulting in faster cooling of the fin surface and a higher water vapor condensation rate, thus causing the frost to grow faster in the vertical direction. As the frost thickens, airflow resistance increases, heat transfer resistance rises, and water vapor diffusion capacity decreases, leading to a gradual slowdown in the frost growth rate, which eventually stabilizes.

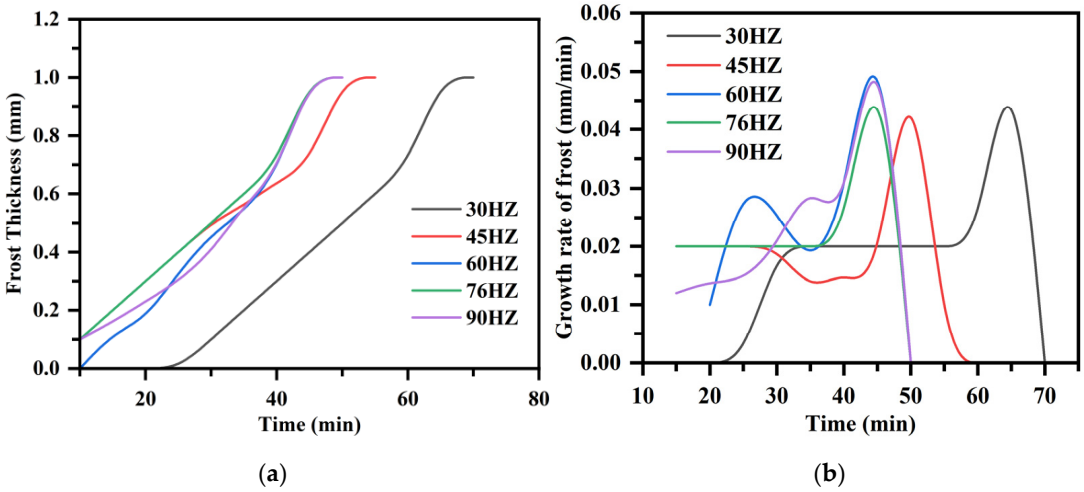


Figure 5. (**a**) Changes in frost thickness with running time at different compressor frequencies with an ambient temperature of 0 °C and a relative humidity of 85%. (**b**) The frost growth rate (mm/min) over time at an ambient temperature of 0 °C under five compressor frequencies (30, 45, 60, 76, and 90 Hz).

The frost growth rate exhibits a non-monotonic variation at different frequencies in Figure 5b. At 45 Hz, the growth rate remains low (≤0.02 mm/min) during the first 40 min, followed by a moderate peak of 0.06 mm/min at 50 min, after which it drops to zero. At higher frequencies (60, 76, and 90 Hz), the growth rate increases significantly after 35 min, reaching peak values of 0.066 mm/min (60 and 90 Hz) and 0.06 mm/min (76 Hz) around 45 min. The subsequent decline in growth rate is primarily because the frost layer has filled the fin gaps; further frost accumulation results in density increase rather than thickness growth. The higher frost growth rate at elevated frequencies can be explained by the increased refrigerant flow rate and lower evaporating temperature, which accelerate frost formation. At 30 Hz, the growth rate remains consistently low (≤0.06 mm/min) with a delayed peak at 65 min, indicating that lower frequencies slow down frosting but do not prevent it. Overall, Figure 5b clearly demonstrates that increasing compressor frequency accelerates frosting, with the most pronounced effects observed in the 60–90 Hz range.

Figure 6 shows the changes in unit heating capacity, unit power consumption, COP, and air-coil surface temperature difference with operating time at different compressor frequencies. Five frequency settings were set: 30 Hz, 45 Hz, 60 Hz, 76 Hz, and 90 Hz, with an ambient temperature of 0 °C and a relative humidity of 85%. Figure 6a reflects the dynamic process of unit heating capacity changing with frequency. The initial heating capacity is

positively correlated with the compressor frequency. The higher the frequency (e.g., 90 Hz), the stronger the initial heating capacity, but the decrease in heating capacity is also more significant. At lower frequencies (e.g., 30 Hz), the initial heating capacity is smaller, but its decrease is more gradual. In the early stage of frosting, the growth of the frost layer under high-frequency conditions enhances the heat transfer capacity of the fin surface to some extent, resulting in a temporary increase in heating capacity. As the frost layer continues to accumulate, the airflow resistance increases and the thermal resistance rises, causing the heating capacity to show a downward trend under all operating conditions. Among them, the heating capacity declines most rapidly at 76 Hz due to the highest frosting rate. Ultimately, as frost growth stabilizes, the rate of decrease in heating capacity at each frequency gradually slows down and remains at a certain equilibrium level.

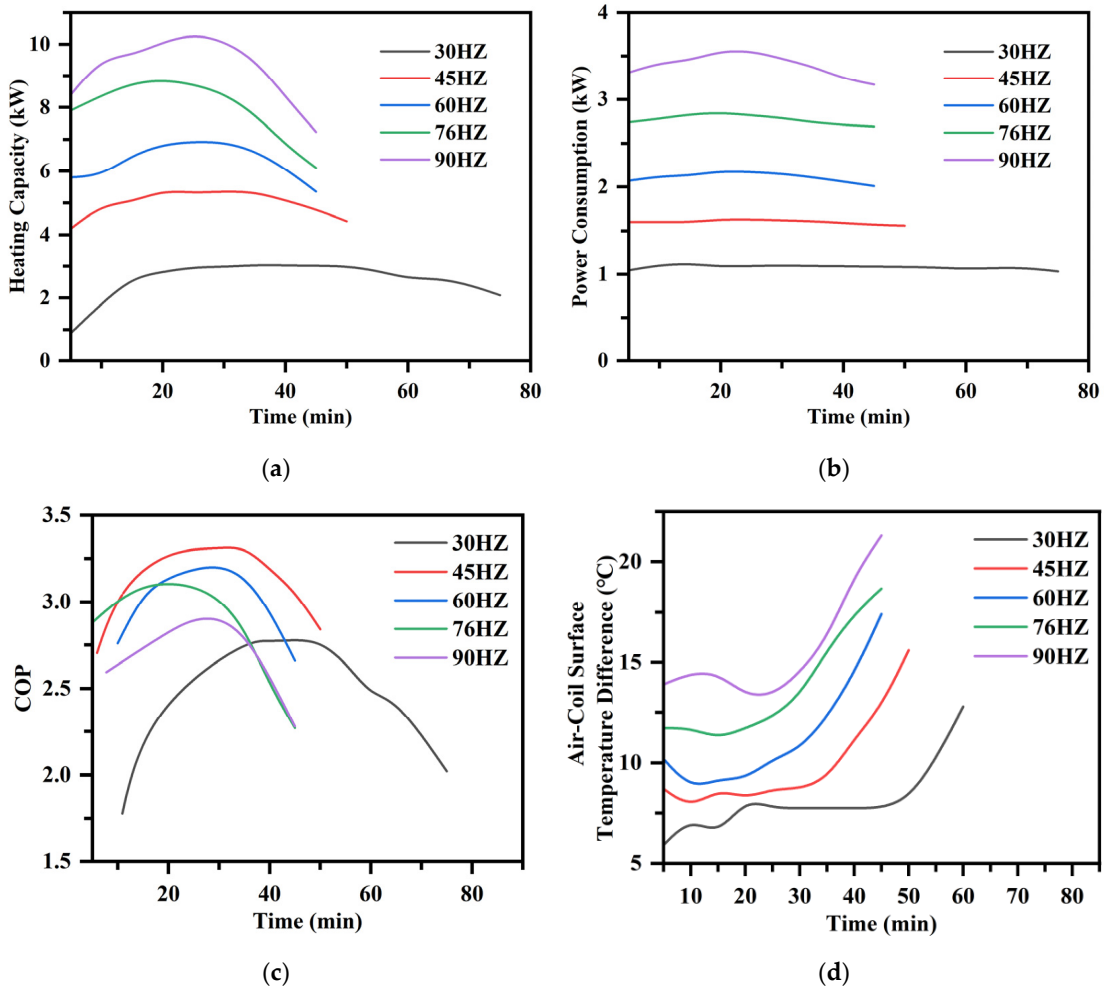


Figure 6. Changes in (**a**) unit heating capacity, (**b**) unit power consumption, (**c**) COP, and (**d**) air-coil surface temperature difference over operating time at different compressor frequencies with an ambient temperature of 0 °C and a relative humidity of 85%.

Figure 6b depicts the power consumption characteristics of the heat pump unit during the frosting process at different compressor frequencies. Overall, the unit's power consumption increases with increasing frequency, and at all frequencies, it shows a slow decreasing trend as the frosting process progresses. The underlying mechanism is that increasing the compressor frequency directly increases the refrigerant's mass flow rate and compression ratio, leading to a significant increase in power consumption. However, as the frost layer accumulates, the thermal resistance on the evaporator side increases, causing a decrease in evaporation temperature and pressure, further expanding the system pressure ratio.

Simultaneously, the refrigerant flow rate also decreases. These two factors work together to gradually reduce the compressor's power consumption. At high-frequency operating conditions (e.g., 90 Hz), the power consumption decrease is more pronounced; while at low-frequency operating conditions (e.g., 30 Hz), due to the slow frost growth, the power consumption remains at a low level and changes relatively gradually.

As shown in the figure, the COP changes over time at different frequencies, indicating that the system performance coefficient exhibits a non-monotonic change characteristic of first increasing and then decreasing throughout the frosting cycle, consistent with the decay pattern of heating capacity (Figure 6c). This is because the heating benefit brought about by enhanced heat exchange in the early stage of frosting exceeds the slow increase in power consumption, leading to an increase in COP; while in the later stage of frost accumulation, the decrease in airflow and the deterioration of heat transfer intensify, resulting in a significant decrease in heating capacity and a subsequent decrease in COP. On the other hand, frequency has a significant impact on COP: when the frequency is too low, the refrigerant mass flow rate is insufficient, limiting the heating capacity; when the frequency is too high, the compressor power consumption increases sharply, and the energy efficiency ratio decreases. Therefore, the COP shows a trend of first increasing and then decreasing with frequency, reaching its maximum value at 45 Hz, indicating that this frequency achieves the optimal balance between heating capacity and power consumption in the current system.

Figure 6d illustrates the variation in the temperature difference between the air and the coil surface during the frosting process of a heat pump at different compressor frequencies over time. Overall, the air-to-coil temperature difference exhibits a typical non-monotonic variation characteristic with operating time: in the initial stage of frosting, the increased fin surface roughness due to frost growth enhances heat exchange to some extent, leading to a brief, slight decrease in temperature difference; however, as frost accumulates, airflow is significantly reduced due to duct blockage, resulting in a sharp deterioration in heat exchange performance. Simultaneously, the evaporation temperature gradually decreases, causing the temperature difference between the coil surface and the air to continuously increase, with the rate of increase gradually accelerating. Higher frequencies result in a larger refrigerant circulation per unit time and a greater heat exchange between the system and the air. However, under conditions of severe frosting leading to deteriorated heat exchange, the higher heat flux density exacerbates the heat transfer imbalance, resulting in a lower coil surface temperature and a significantly larger temperature difference between the coil and the air. Therefore, the temperature difference increases most dramatically at high frequencies (e.g., 90 Hz), while the temperature difference changes relatively gradually at low frequencies (e.g., 30 Hz).

Figure 7 illustrates the relationship between the coefficient of performance (COP) of an air-source heat pump unit and the air-to-coil temperature difference (ΔT) at different compressor frequencies under a fixed ambient temperature. The figure contains six subplots corresponding to different temperature conditions: (a) 6 °C, (b) 3 °C, (c) 0 °C, (d) −3 °C, (e) −6 °C, (f) −9 °C, and (g) −12 °C. Overall, for any fixed frequency, COP exhibits a single-peak trend of first increasing and then decreasing with increasing ΔT. However, the critical temperature difference corresponding to the peak value and the peak COP value differ significantly depending on the frequency. A key phenomenon is that the critical air-to-coil temperature difference corresponding to the optimal COP value also tends to increase with increasing compressor frequency. The main reason for this phenomenon is that increasing the frequency directly increases the refrigerant circulation flow rate and the system's heating capacity. At higher frequencies (such as 76 Hz or 90 Hz), the system requires a stronger heat exchange driving force (i.e., a larger temperature difference ΔT)

to fully realize its enhanced heating potential and overcome the significantly increased compressor power consumption due to high-frequency operation, thereby reaching the optimal COP. Therefore, the optimal COP for high-frequency operation occurs at a larger ΔT. Conversely, at low frequencies (such as 30 Hz), the refrigerant flow is smaller, and the system requires less heat exchange driving force, so its optimal COP can be achieved at a smaller ΔT. Taking 0 °C as an example, the peak COP at 45 Hz is higher than at other frequencies, indicating that the system achieves the best balance between heating capacity and power consumption under this mid-frequency condition. However, when the frequency increases to 76 Hz and 90 Hz, although the heating capacity is enhanced, the compressor power consumption increases sharply, resulting in a more significant decrease in COP in the high ΔT region and a rapid deterioration in system energy efficiency. In contrast, the COP curve changes relatively smoothly when operating at a low frequency of 30 Hz, with a low peak value and a wide distribution range. This is because the heat transfer intensity is limited at low refrigerant flow rates, and the system performance is less sensitive to air-to-coil temperature difference changes.

In summary, the compressor frequency not only determines the peak value of COP but also significantly affects the critical temperature difference required to achieve this optimal performance by changing the system's thermal balance and frosting characteristics.

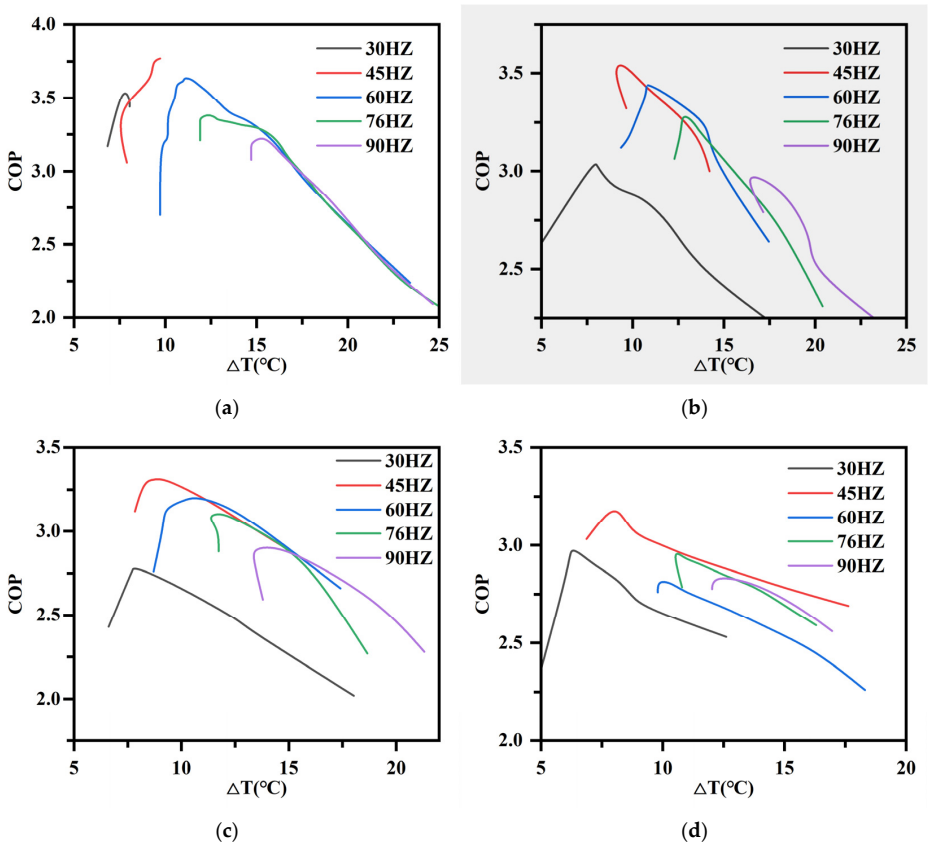


Figure 7. *Cont.*

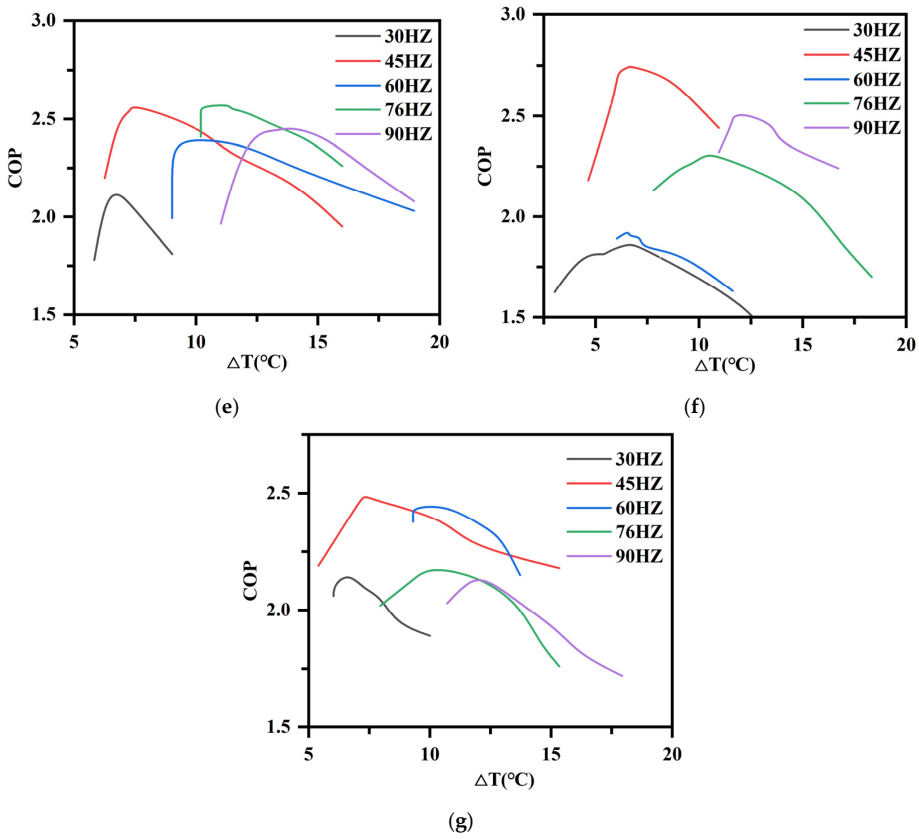


Figure 7. Changes in COP of the unit with air-to-coil temperature difference at different frequencies at a fixed temperature: (**a**) 6 °C, (**b**) 3 °C, (**c**) 0 °C, (**d**) −3 °C, (**e**) −6 °C, (**f**) −9 °C and (**g**) −12 °C.

3.3. The Influence of Ambient Humidity

This study selected a 10% COP reduction as the criterion for unit defrosting to investigate the impact of ambient humidity on the defrosting trigger point under fixed-frequency (76 Hz) operation. As shown in Figure 8, at different ambient temperatures (3 °C, 0 °C, −6 °C), the key parameter characterizing evaporator heat transfer deterioration—the air-to-coil temperature difference—showed only a slight change with increasing ambient humidity, with an overall change rate of within 5%. This result indicates that although the frosting rate and frost accumulation are significantly affected by humidity, humidity is not a major influencing factor for determining the critical performance point of severe COP decline. This critical air-to-coil temperature difference is mainly determined by ambient temperature and compressor frequency; changes in humidity have a negligible impact and can be considered a secondary factor when formulating defrosting control strategies.

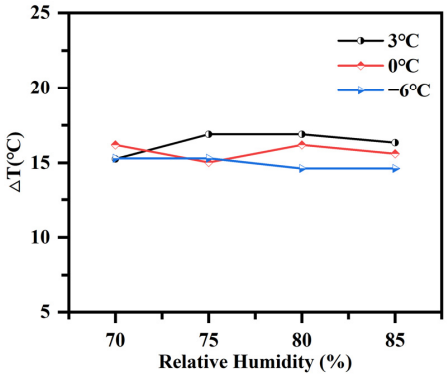


Figure 8. Air-to-coil temperature difference with relative humidity at a fixed frequency (76 Hz) and different ambient temperatures (3 °C, 0 °C, −6 °C) when the unit's COP is 10% lower than the initial COP.

3.4. Establishment of Temperature–Frequency Two-Factor Fitting Model

Based on the summary and analysis of previous experimental data, this study determined that outdoor ambient temperature (t) and compressor frequency (f) are the two most significant factors affecting the critical air-to-coil temperature difference (ΔT) and established defrosting judgment conditions based on these. As shown in Table 6, this table summarizes the operating time and critical temperature difference (ΔT) corresponding to a 10% COP reduction under different frosting ambient temperatures and compressor frequency conditions. The 10% COP reduction threshold was selected based on both engineering practice and the physical characteristics of the frosting process observed in the present experiments. In the field of ASHP defrosting control, a 10–15% reduction in heating capacity or COP is widely recognized as a reasonable criterion for initiating defrosting, because it represents a clear performance degradation while still avoiding excessive frost accumulation that could lead to system instability or safety issues (e.g., compressor liquid hammer). This value has been used in previous studies, such as by Klingebiel et al. [4], who adopted a 10% efficiency loss as the reference for evaluating defrosting controllers, and by Li et al. [14], who used a similar threshold to determine the optimal defrosting start time.

By fitting the data in the table, a dual-partition judgment function with outdoor ambient temperature and compressor frequency as independent variables was finally obtained, namely the critical air-to-coil temperature difference fitting formula:

$$\begin{aligned}\Delta \mathrm{T} = f(t,\ f) = \quad & (-43.8829921) + 0.109479735 \times f + 0.1874247533 \times (t \\ & +273) + (f - 61.575757576) \times ((t + 273 \\ & -269.45454545) \times 0.0009807284).\end{aligned}$$

A multivariate linear regression using the ordinary least-squares method was applied, with a model structure that includes linear terms for ambient temperature (t) and compressor frequency (f) as well as an interaction term $(f - f_0)(t - t_0)$ to capture their coupling effect. The regression was performed using standard statistical software on a data set of 33 valid points, covering five compressor frequencies (30, 45, 60, 76, 90 Hz) and seven ambient temperatures (6, 3, 0, −3, −6, −9, −12 °C) at 85% relative humidity; two points (45 Hz/6 °C and 30 Hz/6 °C) were excluded because no significant COP drop occurred. The coupling term adjusts the baseline linear prediction to match the experimental observation that raising the frequency at low temperatures causes a larger-than-additive increase in ΔT. For example, at −12 °C, increasing the frequency from 30 Hz to 90 Hz raises ΔT from 8.62 °C to 13.72 °C—a difference that the linear terms alone would underestimate. The positive 0.0009807284 thus captures the synergistic amplification of frequency effects at low temperatures, i.e., the more severe frosting caused by a high frequency in a cold environment.

To quantitatively evaluate the predictive accuracy of the proposed dual-factor model, the coefficient of determination (R^2) and the root-mean-square error (RMSE) were calculated based on the experimental data. The definitions are as follows:

$$R^2 = 1 - \frac{\sum_{i=1}^{n}\left(\Delta T_{\mathrm{meas},i} - \Delta T_{\mathrm{pred},i}\right)^2}{\sum_{i=1}^{n}\left(\Delta T_{\mathrm{meas},i} - \overline{\Delta T_{\mathrm{meas}}}\right)^2}$$

$$\mathrm{RMSE} = \sqrt{\frac{1}{n}\sum_{i=1}^{n}\left(\Delta T_{\mathrm{meas},i} - \Delta T_{\mathrm{pred},i}\right)^2}$$

where $\Delta T_{\text{meas},i}$ is the measured critical air-to-coil temperature difference, $\Delta T_{\text{pred},i}$ is the value predicted by the model, $\overline{\Delta T_{\text{meas}}}$ is the mean of the measured values, and n is the number of data points. Using the data listed in Table 6, the calculated R^2 is 0.908, and the RMSE is 0.82 °C. These results demonstrate that the dual-factor model exhibits excellent agreement with experimental measurements, with a prediction error well within the engineering acceptable range.

In addition, based on engineering practice, control thresholds under extreme conditions are defined to avoid defrosting too early or too late. The thresholds are set as follows: (1) running time greater than 20 min; (2) the fan operating current is more than 1.2 times the current when the fan is fully frosted at the corresponding fan frequency and lasts for 5 min. This forms an adaptive intelligent defrosting control technology.

The 20 min minimum run time threshold is derived directly from the experimental data in Table 6. Under the most severe frosting conditions tested, the earliest detected 10% COP reduction occurred at 20 min (at −12 °C, 90 Hz, with ΔT = 13.72 °C). Setting a minimum run time of 20 min ensures that only sustained frosting events—not transient measurement fluctuations—trigger defrosting, thereby avoiding mal-defrost. This value also aligns with the typical compulsory defrost cycle timers used in commercial ASHP controllers.

The outdoor fan employed in the present system is a brushless DC (BLDC) motor with closed-loop speed control. Under normal operation, the controller maintains a nearly constant rotational speed by adjusting the winding current in response to load torque variations. When frost accumulates on the outdoor coil, the increased airflow resistance raises the load torque on the fan. To keep the rotational speed unchanged, the BLDC controller increases the winding current; consequently, the measured fan current rises as frost builds up. For the fan current threshold (1.2 × nominal), the selection is supported by both the physical mechanisms observed in the present experiments and a recent study by Tang et al. [7], who experimentally showed that as frost accumulates on the outdoor coil, the airflow resistance increases, causing the airflow rate to drop and the fan electric current to increase abruptly, leading to fan performance deterioration and a reduction in system heating capacity. Their measurements demonstrated that a 20% increase in fan current corresponds to a substantial airflow blockage and a frost layer thickness that already causes a 10–15% COP decline under standard frosting conditions. The use of fan current as a defrost initiation parameter is further validated by the work of Xu et al. [15], who proposed a frosting state recognition method based on micro-fluctuations in evaporator fan current, achieving recognition accuracy above 94% across a temperature range of −5 to −20 °C. Additionally, the fan current threshold offers a more stable and less ambiguous signal compared to temperature-based methods, which are sensitive to sensor placement and environmental fluctuations.

Table 6. Time and temperature difference when 10% COP reduction for various frosting temperatures and frequencies.

Compressor Frequency f (Hz)	Ambient Temperature t (°C)	Time (min) Required for 10% COP Reduction	Air-to-Coil Temperature Difference (ΔT, °C) When 10% COP Reduction
90	6	45	18.26
90	3	30	19.20
90	0	35	16.20
90	−3	55	16.96
90	−6	40	16.71
90	−9	35	16.72

Table 6. *Cont.*

Compressor Frequency f (Hz)	Ambient Temperature t (°C)	Time (min) Required for 10% COP Reduction	Air-to-Coil Temperature Difference (ΔT, °C) When 10% COP Reduction
90	−12	20	13.72
76	6	70	16.70
76	3	40	15.26
76	0	35	15.60
76	−3	55	15.02
76	−6	55	14.62
76	−9	35	15.18
76	−12	25	13.72
60	6	80	14.70
60	3	55	14.20
60	0	40	14.46
60	−3	40	14.40
60	−6	70	13.96
60	−9	65	11.62
60	−12	40	12.94
45	6	70	--
45	3	60	12.19
45	0	45	12.80
45	−3	60	12.60
45	−6	60	10.20
45	−9	60	10.96
45	−12	45	11.44
30	6	30	--
30	3	95	12.19
30	0	55	10.19
30	−3	100	9.26
30	−6	85	9.03
30	−9	45	9.66
30	−12	80	8.62

Figure 9 compares the measured and model-predicted values of the air-to-coil temperature difference when the unit's 10% COP reduction occurs under different frequency and ambient temperature conditions. Data analysis shows that the prediction results of the two-factor fitting model based on ambient temperature and compressor frequency are in good agreement with the measured values. The vast majority of data points are evenly distributed on both sides of the model's calculated value, indicating high prediction accuracy. Calculations show that the maximum deviation between the predicted and measured values under all operating conditions does not exceed 10%, which is acceptable for engineering applications, fully verifying the effectiveness and reliability of the fitting formula $\Delta T = f(t, f)$.

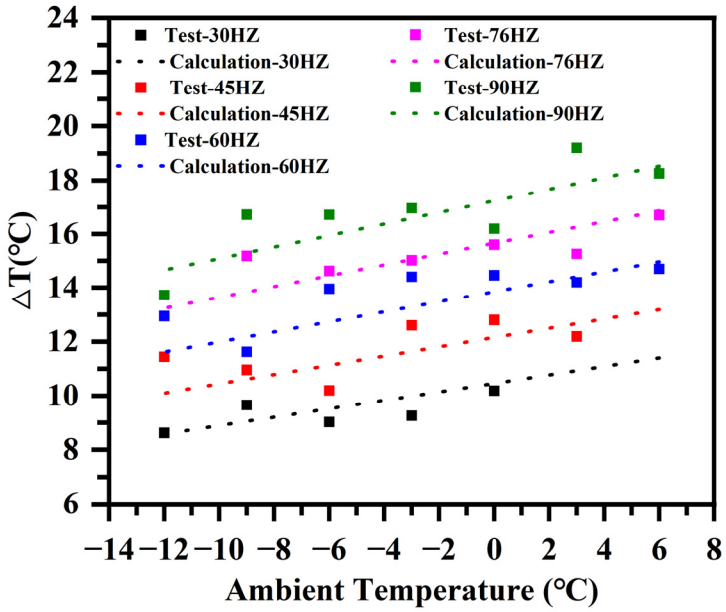


Figure 9. Comparison of measured and calculated values of air-to-coil temperature difference when the unit 10% COP reduction at different frequencies and ambient temperatures (6 °C, 3 °C, 0 °C, −3 °C, −6 °C, −9 °C, and −12 °C).

3.5. Validation of the Temperature–Frequency Two-Factor Fitting Model

3.5.1. Single-Factor Validation

Figure 10a shows the comparison between the measured and model predicted values of the air-to-coil temperature difference when the unit 10% COP reduction under a fixed ambient temperature of 0 °C, by additionally designing multiple frequency conditions such as 40, 55, 70, and 85 Hz. It can be seen that the data points at the newly added operating frequencies are evenly distributed on both sides of the reference line and fall entirely within the ±10% error band. This result clearly confirms that, under a single ambient temperature variable, the established critical air-to-coil temperature difference prediction model $\Delta T = f(f) \mid (t = 0\ ^\circ\mathrm{C})$ can accurately capture the influence of different frequency changes on the critical point of system performance. The verification at the added frequency points further strengthens the effectiveness and reliability of the model, providing solid data support for the accurate formulation of defrosting control strategies.

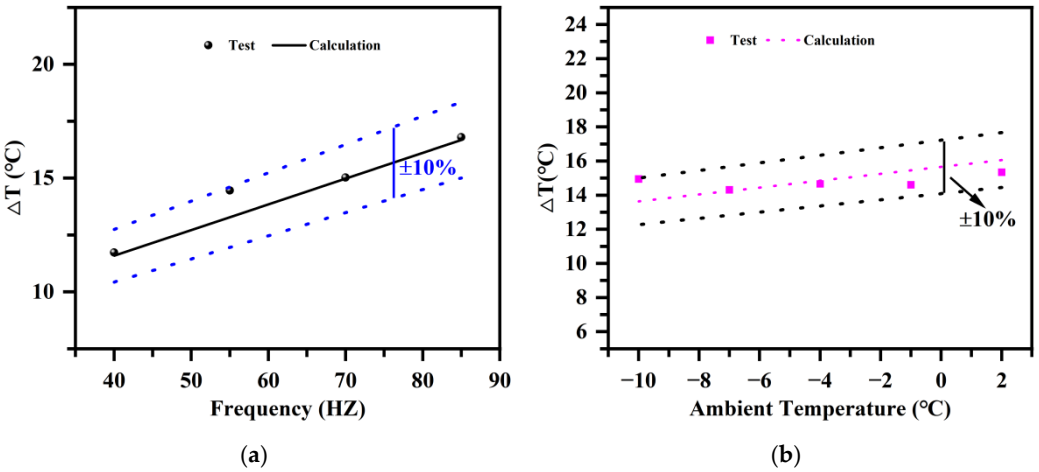


Figure 10. Comparison of measured and calculated values of air-to-coil temperature difference when the unit 10% COP reduction at a fixed ambient temperature of 0 °C (**a**) and at a fixed frequency of 76 Hz (**b**).

Figure 10b shows the comparison between the measured and model-predicted values of the air-to-coil temperature difference corresponding to a 10% COP reduction when the ambient temperature changes, under the condition that the compressor frequency is fixed at 76 Hz. Test data from multiple temperature conditions, including 2 °C, −1 °C, −4 °C, −7 °C, and −10 °C, show that the measured values at all temperatures are highly consistent with the model calculations and are evenly distributed on both sides of the reference line, falling entirely within the ±10% error range. This result further confirms that, under a fixed frequency variable, the established critical temperature difference prediction model ΔT= f(t) | (f = 76 HZ) can accurately reflect the effect of different ambient temperatures on the critical point of system performance. The validation at the added temperature points significantly enhances the model's applicability and reliability over a wide temperature range, providing a more comprehensive theoretical basis for the accurate formulation of defrosting control strategies under complex operating conditions.

3.5.2. Two-Factor Validation

Based on the above experiments, further verification tests were conducted under coupled conditions of multiple factors (relative humidity, ambient temperature, and compressor frequency). By setting the relative humidity to 85% (Tables 7–9) and 75% (Tables 10–12), and the ambient temperature to 0 °C (Tables 7 and 10), −3 °C (Tables 8 and 11), and −6 °C (Tables 9 and 12), and allowing the heat pump to run freely in variable frequency mode (temperature fluctuation controlled within ±2 °C), the system collected measured data of the air-to-coil temperature difference under different operating conditions and compared them with the model prediction values. The results are shown in the Tables 7–12. The results show that under coupled operating conditions where ambient temperature (0 °C, −3 °C, −6 °C), relative humidity (75%, 85%), and compressor frequency (58–90 Hz) change together, the established critical air-to-coil temperature difference prediction model (ΔT = f (t, f)) exhibits good engineering applicability and prediction accuracy. Specifically, in different combinations of operating conditions, when the deviation between the measured value and the calculated value of the air-to-coil temperature difference is within 12%, the system COP decrease rate is stably maintained at around 10%. This result verifies that the model can accurately capture the critical decay point of system performance during the frosting process. Most importantly, the data comparison under the same temperature and different humidity conditions shows that the humidity change did not have a significant impact on the critical air-to-coil temperature difference, which further strengthens the reliability of the model with temperature and frequency as the core criteria and provides solid data support and theoretical basis for the formulation of intelligent defrosting control strategies under complex actual conditions.

Table 7. The air-to-coil temperature difference under variable frequency operating conditions with ambient temperature 0 ± 2 °C and relative humidity 85%, compared with model predictions.

Time	Ambient Temperature (°C)	Control Value ΔT (°C)	ΔT (Converted from Measured Pressure) (°C)	Difference from Control Value	Frost Layer Thickness (mm)	COP	COP Decline
19:33	−0.45	15.56	10.76	−30.87%		2.52	14.58%
19:38	−0.14	15.63	10.56	−32.45%	micro-hang	2.68	9.15%
19:43	−1.25	15.40	11.01	−28.52%	0.1	2.66	9.83%
19:48	−1.88	15.28	10.92	−28.54%	0.2	2.62	11.19%
19:53	1.32	15.92	11.51	−27.72%	0.3	2.85	3.39%
19:58	1.89	16.04	12.08	−24.68%	0.4	2.95	0.00%
20:03	0.39	15.73	12.65	−19.60%	0.5	2.85	3.39%
20:08	−0.03	15.65	12.77	−18.42%	0.6	2.7	8.47%

Table 7. *Cont.*

Time	Ambient Temperature (°C)	Control Value Δ*T* (°C)	Δ*T* (Converted from Measured Pressure) (°C)	Difference from Control Value	Frost Layer Thickness (mm)	COP	COP Decline
20:13	−0.22	15.61	14.24	−8.80%	0.7	2.62	11.19%
20:18	−0.35	15.58	15.85	1.68%	Full	2.44	17.29%
20:23	0.1	15.67	18.12	15.63%		2.33	21.02%
20:28	0.01	13.85	13.90	0.40%		1.87	36.61%

Table 8. The air-to-coil temperature difference under variable frequency operating conditions with ambient temperature of −3 ± 2 °C and relative humidity of 85%, compared with model predictions.

Time	Frequency	Ambient Temperature (°C)	ΔT Calculation (°C)	ΔT (Pressure Conversion) (°C)	Difference from Control Value	Frost Layer Thickness (mm)	COP	COP Decline
14:20	76	−3.15	15.02	10.19	−32.15%	0.1	2.4	13.36%
14:25	76	−3.19	15.01	10.70	−28.69%	0.25	2.63	5.05%
14:30	76	−4.42	14.76	10.61	−28.16%	0.35	2.6	6.14%
14:35	76	−1.9	15.27	9.83	−35.63%	0.4	2.73	1.44%
14:40	76	−2.13	15.23	11.76	−22.73%	0.5	2.77	0.00%
14:45	76	−3.14	15.02	10.75	−28.41%	0.6	2.66	3.97%
14:50	76	−2.74	15.10	12.29	−18.64%	0.7	2.69	2.89%
14:55	76	−3.09	15.03	13.11	−12.81%	0.75	2.58	6.86%
15:00	76	−2.92	15.07	14.48	−3.86%	Full	2.5	9.75%
15:05	76	−2.93	15.06	15.09	0.21%		2.35	15.16%
15:10	76	−2.77	15.10	18.54	22.79%		2.21	20.22%

Table 9. The air-to-coil temperature difference under variable frequency operating conditions with ambient temperature of −6 ± 2 °C and relative humidity of 85%, compared with model predictions.

Time	Frequency	Ambient Temperature (°C)	ΔT Calculation (°C)	ΔT (Pressure Conversion) (°C)	Difference from Control Value	Frost Layer Thickness (mm)	COP	COP Decline
17:05	70	−6	13.80	9.61	−30.40%	micro-hang	2.08	19.69%
17:10	76	−6.47	14.35	9.14	−36.34%	0.1	2.33	10.04%
17:15	76	−7.39	14.16	10.01	−29.30%	0.2	2.32	10.42%
17:20	76	−5.12	14.62	8.77	−39.99%	0.3	2.53	2.32%
17:25	76	−4.87	14.67	10.74	−26.83%	0.4	2.59	0.00%
17:30	76	−6.41	14.36	10.38	−27.70%	0.5	2.49	3.86%
17:35	76	−7.17	14.21	10.23	−27.97%	0.6	2.43	6.18%
17:40	76	−5.82	14.48	10.38	−28.35%	0.65	2.5	3.47%
17:45	76	−5.98	14.45	11.42	−20.93%	0.7	2.52	2.70%
17:50	76	−6.09	14.43	11.93	−17.27%	0.75	2.5	3.47%
17:55	76	−6.06	14.43	12.60	−12.72%	Full	2.45	5.41%
18:00	76	−6.01	14.44	14.61	1.19%		2.4	7.34%
18:05	64	−6.04	13.15	8.99	−31.68%		1.94	25.10%
18:10	58	−5.77	12.56	11.63	−7.37%		1.57	39.38%

Table 10. The air-to-coil temperature difference under variable frequency operating conditions with ambient temperature 0 ± 2 °C and relative humidity 75%, compared with model predictions.

Time	Frequency	Ambient Temperature (°C)	ΔT Calculation (°C)	ΔT (Pressure Conversion) (°C)	Difference from Control Value	Frost Layer Thickness (mm)	COP	COP Decline
12:56	76	−0.33	15.59	9.86	−36.76%		2.57	13.76%
13:01	76	−0.1	15.63	10.60	−32.23%	micro-hang	2.78	6.71%
13:06	76	−0.67	15.52	11.06	−28.73%	0.1	2.79	6.38%
13:11	76	−2.02	15.25	10.78	−29.32%	0.2	2.76	7.38%
13:16	76	−1.2	15.41	11.60	−24.76%	0.3	2.78	6.71%
13:21	76	1.54	15.96	11.23	−29.67%	0.4	2.98	0.00%
13:26	76	1.65	15.99	12.35	−22.78%	0.45	2.93	1.68%
13:31	76	−0.09	15.64	12.71	−18.74%	0.5	2.73	8.39%
13:36	76	−0.39	15.58	12.95	−16.85%	0.6	2.71	9.06%
13:41	76	−0.18	15.62	13.71	−12.19%	0.7	2.69	9.73%
13:46	76	0.08	15.67	15.69	0.10%	0.75	2.65	11.07%
13:51	64	−0.26	14.25	9.93	−30.33%	Full	2.55	14.43%
13:56	58	0.05	13.63	13.39	−1.75%		1.62	45.64%

Table 11. The air-to-coil temperature difference under variable frequency operating conditions with ambient temperature of −3 ± 2 °C and relative humidity of 75%, compared with model predictions.

Time	Frequency	Ambient Temperature (°C)	ΔT Calculation (°C)	ΔT (Pressure Conversion) (°C)	Difference from Control Value	Frost Layer Thickness (mm)	COP	COP Decline
15:11	76	−3.08	15.03	10.81	−28.07%		2.47	12.72%
15:16	76	−3.54	14.94	11.49	−23.12%	micro-hang	2.53	10.60%
15:21	76	−4.53	14.74	11.67	−20.87%	0.1	2.62	7.42%
15:26	76	−4.89	14.67	10.72	−26.95%	0.15	2.6	8.13%
15:31	76	−4.11	14.83	10.35	−30.22%	0.2	2.67	5.65%
15:36	76	−1.56	15.34	11.24	−26.75%	0.25	2.83	0.00%
15:41	76	−1.8	15.29	11.54	−24.53%	0.3	2.78	1.77%
15:46	76	−2.82	15.09	11.64	−22.87%	0.4	2.76	2.47%
15:51	76	−3.53	14.94	11.50	−23.06%	0.5	2.68	5.30%
16:06	76	−3.66	14.92	11.37	−23.80%	0.55	2.67	5.65%
16:01	76	−4.03	14.84	11.58	−22.01%	0.6	2.61	7.77%
16:06	76	−3.07	15.04	11.39	−24.27%	0.7	2.67	5.65%
16:11	76	−2.41	15.17	13.20	−13.00%	0.75	2.69	4.95%
16:16	76	−2.99	15.05	13.21	−12.27%	Full	2.62	7.42%
16:21	76	−3.46	14.96	13.33	−10.85%		2.57	9.19%
16:26	36	−3.14	10.63	6.55	−38.39%		2.54	10.25%
16:31	58	−2.97	13.08	10.37	−20.68%		2.27	19.79%

Table 12. The air-to-coil temperature difference under variable frequency operating conditions with ambient temperature of −6 ± 2 °C and relative humidity of 75%, compared with model predictions.

Time	Frequency	Ambient Temperature (°C)	ΔT Calculation (°C)	ΔT (Pressure Conversion) (°C)	Difference from Control Value	Frost Layer Thickness (mm)	COP	COP Decline
18:12								
18:17	70	−5.72	13.86	9.31	−32.84%		2.23	18.32%
18:22	76	−6.17	14.41	10.03	−30.43%	micro-hang	2.28	16.48%
18:27	76	−7.42	14.16	9.98	−29.48%	0.1	2.31	15.38%
18:32	76	−7.57	14.13	10.45	−26.00%	0.2	2.35	13.92%

Table 12. *Cont.*

Time	Frequency	Ambient Temperature (°C)	ΔT Calculation (°C)	ΔT (Pressure Conversion) (°C)	Difference from Control Value	Frost Layer Thickness (mm)	COP	COP Decline
18:37	76	−6.8	14.28	9.99	−30.03%	0.25	2.45	10.26%
18:42	76	−4.8	14.69	10.23	−30.37%	0.3	2.56	6.23%
18:47	76	−4.2	14.81	12.00	−18.99%	0.35	2.66	2.56%
18:52	76	−6.28	14.39	11.12	−22.69%	0.4	2.52	7.69%
18:57	76	−7.33	14.18	10.69	−24.56%	0.5	2.40	12.09%
19:02	76	−6.72	14.30	10.68	−25.28%	0.6	2.45	10.26%
19:07	76	−6.06	14.43	11.34	−21.40%	0.65	2.49	8.79%
19:12	76	−6.11	14.42	11.91	−17.39%	0.7	2.48	9.16%
19:17	76	−6.13	14.42	11.89	−17.50%	0.75	2.73	0.00%
19:22	76	−6.19	14.41	12.47	−13.47%	0.78	2.44	10.62%
19:27	76	−6.01	14.44	13.29	−7.98%	Full	2.42	11.36%
19:32	76	−6.15	14.41	14.47	0.41%		2.35	13.92%
19:37	58	−5.91	12.53	9.12	−27.27%		1.99	27.11%

3.6. Comparison with Traditional Defrost Strategies

To further highlight the advantages of the proposed dual-factor defrosting model, a systematic comparison with representative traditional defrost strategies is provided in Table 13. These strategies include the conventional time–temperature (T-T) method [16], a pressure-based approach using differential pressure sensors [8], and two AI-based methods: deep reinforcement learning [9] and image gray recognition [11].

Table 13. Comparison of the proposed model with traditional defrost strategies.

Strategy Type	Representative Study	Key Features/Input Parameters	Advantages	Limitations
Time-based (T-T)	Conventional method (Liu et al., 2017) [16]	Temperature threshold (−3 °C) + fixed time (60 min)	Simple, low cost	Cannot adapt to variable frosting conditions; mal-defrost rate high (68% reported)
Pressure-based	Chung et al. (2019) [8]	Differential pressure sensor across evaporator	Directly reflects airflow blockage	Requires additional sensor; prediction error ~5.5% but limited to specific heat exchangers
AI-based (deep reinforcement learning)	Klingebiel et al. (2025) [9]	Standard temperature sensors; self-optimizing	Adaptive; improves seasonal efficiency by 7.1–9.1%	Computationally intensive; requires training; black-box model
AI-based (image gray recognition)	Wang et al. (2024) [11]	Camera; image grayscale processing	High defrosting accuracy (93.33%); COP +36.6%	Requires camera and image processing hardware; lighting sensitivity
Proposed model (this work)	Dual-factor model $\Delta T = f(t, f)$	Ambient temperature (t) and compressor frequency (f)	No extra sensors needed; physically transparent; captures temperature–frequency coupling; prediction error < 10%; $R^2 = 0.908$	Limited to inverter-driven ASHPs; model constants specific to tested unit

As shown in Table 13, the conventional T-T method is simple and low-cost, but its inability to adapt to variable frosting conditions leads to a high mal-defrost rate (up to 68% [16]). The pressure-based method offers a direct measure of airflow blockage, yet it requires an additional sensor, and its prediction error (≈5.5%) is only validated for specific heat exchanger geometries [8]. AI-based methods achieve notable performance gains-for instance, the image gray recognition equipment (IGRE) improves defrosting accuracy by 42.86% and COP by 36.60% compared to T-T control [11]. However, these methods demand extra hardware (cameras, processors) and computational resources, and their black-box nature makes physical interpretation difficult.

In contrast, the proposed dual-factor model offers several distinct advantages. First, it requires no additional sensors beyond those already present in a standard ASHP (temperature and pressure transducers). Second, the model is physically transparent: the cross-term coefficient explicitly quantifies the coupling effect between ambient temperature and compressor frequency. Third, its predictive performance is excellent, with R^2 = 0.908, RMSE = 0.82 °C, and a prediction error below 10% across all tested conditions. These features make the model a practical, low-cost, and accurate tool for on-demand defrosting control in inverter-driven ASHPs, especially when compared to more complex or less adaptive conventional strategies.

4. Conclusions

This study investigated frosting and performance degradation of air-source heat pumps (ASHPs). A controlled environmental platform was used. The coupled effects of ambient temperature and compressor frequency were revealed. Key findings are as follows: (1) Frost accumulation was most severe near 0 °C. Increased thermal resistance caused a decline in heating capacity and COP. (2) Higher compressor frequencies enhanced initial heating capacity. However, they also accelerated frosting and performance deterioration. An optimal energy efficiency balance was found at approximately 45 Hz for the tested system. (3) Relative humidity had a negligible effect on the critical ΔT at the 10% COP reduction threshold. Its variation was less than 5%. Thus, relative humidity is a secondary factor in defrosting control. (4) A dual-factor prediction model for critical defrosting ΔT was developed. The model uses ambient temperature (t) and compressor frequency (f) as independent variables. The model showed high reliability. Its prediction error was below 10% in both single-factor and multi-factor tests. Collectively, this research provides a theoretical framework and a practical engineering tool. These can help optimize intelligent defrosting strategies. They can also enhance the operational stability of variable-frequency ASHPs under complex climates.

Author Contributions: X.X.: conducted the experiments and wrote the original draft. Investigation. T.Z.: developed the methodology and revised the manuscript. D.L.: prepared the figures and reviewed the manuscript. W.S.: performed validation. Z.W. provided resources and curated data. Y.X.: conceived the study, supervised the project, and acquired funding. All authors have read and agreed to the published version of the manuscript.

Funding: This project was supported by the National Natural Science Foundation of China (No. 52506002), the Guangdong Provincial University Youth Innovation Talent Program (No. 2024KQNCX171), and the Foshan Innovation Research Project (No. 2024JNHB01).

Data Availability Statement: The original contributions presented in the study are included in the article, further inquiries can be directed to the corresponding author.

Conflicts of Interest: The authors declare no competing financial interests.

References

1. Dong, S.; Zhao, H.; Zheng, Y.; Ni, L. Carbon reduction analysis of electric heat pumps in carbon neutrality in China. *Sustain. Cities Soc.* **2023**, *97*, 104758. [CrossRef]
2. Ma, L.; Sun, Y.; Wang, F.; Wang, M.; Zhang, S.; Wang, Z. Advancements in anti-frosting and defrosting techniques for air source heat pumps: A comprehensive review of recent progress. *Appl. Energy* **2025**, *377*, 124358. [CrossRef]
3. Qu, M.; Zhang, R.; Chen, J.; Cheng, Y.; Zhao, X.; Zhang, T.; Li, Z. Experimental analysis of heat coupling during TES based reverse cycle defrosting method for cascade air source heat pumps. *Renew. Energy* **2020**, *147*, 35–42. [CrossRef]
4. Klingebiel, J.; Höges, C.; Göbel, S.; Bannmüller, P.; Boelsen, T.; Venzik, V.; Vering, C.; Müller, D. Optimal defrost initiation for air-source heat pumps: Evaluating the improvement potential of common defrosting controllers. *Energy* **2025**, *324*, 135871. [CrossRef]
5. Liu, S.; Bai, X.; Deng, S.; Zhang, L.; Wei, M. Developing a novel control strategy for frosting suppression based on condensing-frosting performance maps for variable speed air source heat pumps. *Energy Build.* **2023**, *289*, 113049. [CrossRef]
6. Wang, S.; Wei, W.; Luo, J.; Wang, W.; Sun, Y.; Li, Z.; Huang, C.; Tang, R.; Deng, S. A prediction model of the optimal defrosting initiating time for the air source heat pumps with different configurations and operations. *Energy Build.* **2025**, *326*, 115079. [CrossRef]
7. Tang, R.; Wei, W.; Sun, P.; Zhao, J.; Wang, W.; Sun, Y.; Deng, S. A novel time-current-temperature difference (T-I-T) defrosting control method for air source heat pump based on outdoor fan operation characteristics in space heating. *Appl. Therm. Eng.* **2025**, *259*, 124850. [CrossRef]
8. Chung, Y.; Na, S.I.; Choi, J.; Kim, M.S. Feasibility and optimization of defrosting control method with differential pressure sensor for air source heat pump systems. *Appl. Therm. Eng.* **2019**, *155*, 461–469. [CrossRef]
9. Klingebiel, J.; Höges, C.; Horst, J.; Nießen, O.; Venzik, V.; Vering, C.; Müller, D. A self-optimizing defrost initiation controller for air-source heat pumps: Experimental validation of deep reinforcement learning. *Appl. Energy* **2025**, *398*, 126400. [CrossRef]
10. Guo, Y.; Shao, S.; Geng, X.; Li, H.; Wang, Z.; Akkurt, N. A data-driven evaluating method on the defrosting effect of the air source heat pump system in Beijing. *Appl. Therm. Eng.* **2023**, *235*, 121377. [CrossRef]
11. Wang, S.; Wei, W.; Xie, J.; Wang, W.; Sun, Y.; Li, Z.; Lin, Y.; Huang, C.; Deng, S. Space heating performance analysis of air source heat pump integrated with image gray recognition-based defrosting controller. *Appl. Therm. Eng.* **2024**, *236*, 121536. [CrossRef]
12. Zheng, X.; Shi, R.; You, S.; Han, Y.; Shi, K. Experimental study of defrosting control method based on image processing technology for air source heat pumps. *Sustain. Cities Soc.* **2019**, *51*, 101667. [CrossRef]
13. Wei, W.; Ni, L.; Li, S.; Wang, W.; Yao, Y.; Xu, L.; Yang, Y. A new frosting map of variable-frequency air source heat pump in severe cold region considering the variation of heating load. *Renew. Energy* **2020**, *161*, 184–199. [CrossRef]
14. Li, Z.; Wang, W.; Sun, Y.; Liang, S.; Deng, S.; Lin, Y.; Wu, X. A novel defrosting initiating method for air source heat pumps based on the optimal defrosting initiating time point. *Energy Build.* **2020**, *222*, 110064. [CrossRef]
15. Xu, Y.; Zhao, R.; Wu, K.; Jin, H.; Song, M.; Shen, X. Experimental investigation and validation on an air-source heat pump frosting state recognition method based on fan current fluctuation signal and machine learning. *Energy* **2024**, *291*, 130372. [CrossRef]
16. Liu, J.; Sun, Y.; Wang, W.; Zhu, J. Performance evaluation of air source heat pump under unnecessary defrosting phenomena for nine typical cities in China. *Int. J. Refrig.* **2017**, *74*, 385–398. [CrossRef]

Disclaimer/Publisher's Note: The statements, opinions and data contained in all publications are solely those of the individual author(s) and contributor(s) and not of MDPI and/or the editor(s). MDPI and/or the editor(s) disclaim responsibility for any injury to people or property resulting from any ideas, methods, instructions or products referred to in the content.